Journal of Manufacturing Processes 107 (2023) 252–267

Contents lists available at ScienceDirect

Journal of Manufacturing Processes

journal homepage: www.elsevier.com/locate/manpro

Residual stress simulation for bimetallic sleeve roll constructed by shrink-fitting in comparison with bimetallic solid roll

Mohd Radzi Aridi [a,b], Rahimah Abdul Rafar [a], Nao-Aki Noda [a,*], Zifeng Sun [a], Yoshikazu Sano [a], Kakeru Takata [a], Yasushi Takase [a]

[a] Department of Mechanical Engineering, Kyushu Institute of Technology, 1-1 Sensui-cho, Tobata-ku, Kitakyushu 804-8850, Japan
[b] Department of Mechanical Engineering, Universiti Tenaga Nasional, Jalan IKRAM-Uniten, Kajang, Selangor 43000, Malaysia

ARTICLE INFO

Keywords:
Heat treatment
Rolling
Simulations
Shrink-fitting
Sleeve
Shaft

ABSTRACT

Next-generation rolls such as super-cermet rolls can be manufactured only by adopting a sleeve roll structure where the shaft is shrink-fitted into the sleeve. To prevent sleeve cracking due to sleeve slip, reducing the residual stress at the inner surface of the sleeve is important. In this paper, therefore, two extreme manufacturing processes are investigated to provide suitable residual stress to the sleeve; one is the process of quenching/tempering a solid roll and boring the inside to manufacture a sleeve. The other is the process in which the inside of a solid roll is lathed to manufacture a sleeve, which is then quenched/tempered. The results show that the latter sleeve heat treatment is better than the former solid heat treatment because the tensile residual stress can be reduced at the sleeve inside. After shrink-fitting of the shaft into the latter sleeve, the fatigue strength and the residual stress are discussed in comparison with the ones of the solid roll currently and widely used.

1. Introduction

In the steel manufacturing industry, rolling is the most efficient method for high-volume production and provides higher yields than other metalworking processes [1–23]. As for rolling rolls, solid-type rolls in Fig. 1(a) are mainstream, but there is an idea to shift the structure to the sleeve assembly type in Fig. 1(b) where the shaft is shrink-fitted into the hollow cylindrical body. Many sleeve rolls have been tried and some have been put into practical use as backup rolls with a large body diameter exceeding 1000 mm [1] and as work rolls for large H-beams [4,5,24–26]. The sleeve assembly type roll has several advantages;

(1) Maintaining the ductility of the shaft and improving the wear resistance of the sleeve alone
(2) The shaft can be reused by replacing the damaged or worn sleeve
(3) Next-generation rolls such as super-cermet rolls can be manufactured only by adopting this.

Fig. 1(a) illustrates a bimetallic solid roll widely used for hot finish rolling. This is mainly because HSS is excellent in wear resistance, surface roughening resistance, and thermal crack resistance [27]. Fig. 1(b) illustrates a bimetallic sleeve roll investigated in this paper, which has a smaller barrel diameter than larger rolls used for large H-shaped steel rolling. Therefore, the sleeve thickness (D - d′)/2, which is determined from the barrel diameter D and the shaft diameter d′ is small for the sleeve roll in Fig. 1(b), making it difficult to manufacture. However, even in the case of the roll shown in Fig. 1(b), as with the large-sized roll, many prototypes have been made for the assembly structure of the sleeve. As a result, it was found that the biggest problem for practical use is how to solve sleeve cracking and residual bending that occurs in the shaft due to sleeve slippage.

As mentioned above, the sleeve assembly type roll has several peculiar problems such as residual bending deformation, fretting fatigue cracks at the sleeve edge, and sleeve damage due to sleeve slippage [5–11]. In particular, regarding sleeve slippage, it is known that the sleeve slips significantly in the circumferential direction, even though the frictional resistance torque of the shrink-fit portion is greater than the torque of the motor [10–13]. A similar slippage is also known as damage called “interface creep” in rolling bearings, and slippage occurs between the shaft and inner race and between the housing and outer race [28–40] although almost no studies deal with such slip quantitatively. In the authors’ previous studies, therefore, numerical simulations were performed under free rolling. It was found that the interfacial slip is irreversible, and not the entire slip, but the slip that occurs partially in the circumferential direction. Then, such non-uniform irreversible slip

* Corresponding author.
E-mail address: nao592noda@gmail.com (N.-A. Noda).

https://doi.org/10.1016/j.jmapro.2023.09.068
Received 6 July 2022; Received in revised form 13 July 2023; Accepted 13 September 2023
Available online 25 October 2023

Nomenclature

D	work roll's body diameter (mm)
$d^{'}$	work roll's shaft diameter (mm)
r	radius (mm)
z	axial length (mm)
α	heat transfer coefficient
δ	shrink-fitting allowance (mm)
θ	angle (°)
T_{Start}	initial temperature
$T_{Pearlite}$	temperature for the pearlite transformation
T_{Keep}	keeping temperature
$T_{Bainite}$	temperature for the bainite transformation
$T_{Q,Keep}$	keeping temperature during quenching
$T_{T,Finish}$	end temperature after tempering finish
σ_r	radial stress (MPa)
σ_z	axial stress (MPa)
σ_θ	tangential stress (MPa)
σ_{eq}	equivalent von Mises stress (MPa)
σ_m	mean stress (MPa)
σ_a	stress amplitude (MPa)
σ_{res}	residual stress (MPa)
σ_θ	tangential stress (MPa)
P/P_{total}	rolling force ratio
σ_r^{sleeve}	radial stress for sleeve heat treatment type (MPa)
σ_r^{solid}	radial stress for solid heat treatment type (MPa)
σ_θ^{sleeve}	tangential stress for sleeve heat treatment type (MPa)
σ_θ^{solid}	tangential stress for solid heat treatment type(MPa)
σ_{min}	minimum stress (MPa)
σ_{max}	maximum stress (MPa)
σ_{w0}	fatigue limit stress (MPa)
σ_B	ultimate tensile strength (MPa)
τ_{rz}	surface shear stress
SF	safety factor defined as $SF = \overline{OB'}/\overline{OB}$

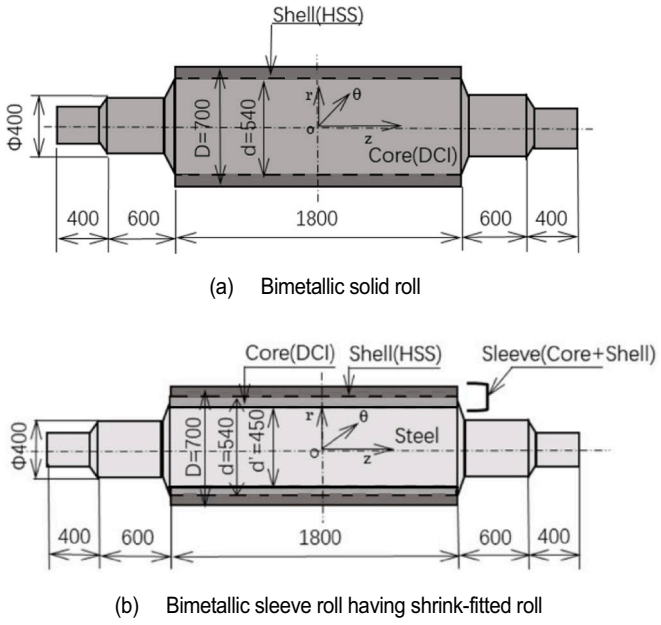

Fig. 1. Solid roll and sleeve roll dimensions (mm).
(a) Bimetallic solid roll.
(b) Bimetallic sleeve roll having shrink-fitted roll.

accumulates with roll rotation and becomes sleeve slip [21]. Furthermore, it was explained that the torque required for rolling greatly accelerated the slip amount [20–22]. The validity of the simulation was confirmed experimentally by using a miniature rolling mill [41].

In this way, the authors clarified several major factors such as rolling load and shrink-fitting conditions affecting this sleeve slippage [19–23,41]. Since sleeve cracking due to sleeve slip may occur from the inner surface of the sleeve, reducing the residual stress on the inner surface of the sleeve is an important issue to solve this problem. Regarding HSS/DCI bimetallic solid rolls (HSS: high-speed steel, DCI: ductile casting iron) in Fig. 1(a), the residual stress was clarified during quenching and tempering through finite element method (FEM) simulations in the previous studies [42–44]. However, regarding HSS/DCI bimetallic sleeve roll in Fig. 1(b), no study is available for the residual stress. The target compressive residual stress at the outer surface can be in the range $\sigma_\theta = 200 \sim 400$ MPa and the target tensile residual stress at the inner surface can be in the range $\sigma_\theta \leq 200$ MPa.

In this study, therefore, two different manufacturing methods will be considered for the bimetallic sleeve roll in Fig. 1(b) to satisfy the suitable residual stress; one is the process of quenching/tempering a solid roll and boring the inside to manufacture a sleeve. The other is the process in which the inside of a solid roll is lathed to manufacture a sleeve, which is then quenched/tempered. After a suitable manufacturing method is clarified, the fatigue risk of the sleeve will be discussed in comparison with the results of the solid bimetallic roll in Fig. 1(a) to confirm the validity of the residual stress.

2. Analysis method

2.1. Previous studies of residual stress for work roll

Previously, the residual stress was mainly measured experimentally by applying proposed methods for residual stress [45]. Destructive mechanical methods include deep hole drilling method, Sachs boring method and slitting method [46–49], and non-destructive methods include X-ray diffraction method and Ultrasonic method [50,51]. However, the experimental method is time-consuming, costly, and requires damage to experimental components. Especially for large-scale bimetallic roll, destructive methods are always limited by measuring accuracy, and non-destructive methods are limited by measuring depth. Despite many studies focused on residual stress caused by quenching in the past decades, most studies dealt with small-size components [52–55]. Recently, Torres et al. analyzed bimetallic work rolls during the post-casting cooling stage [56]. In the authors' previous studies, a thermo-elastic-plastic finite element simulation was performed to investigate the residual stress during quenching [17]. Then, the effects of the shell–core ratio, diameter, phase transformation, and material heat treatment process on the residual stress were discussed. The non-uniform heating and quenching method was found to be useful for reducing the risk of failure by decreasing the center tensile stress without decreasing the surface compressive stress [17,44]. Considering creep behavior, the tempering effect causing residual stress reduction was also clarified [57]. In this study, the analysis method for residual stress will be applied to the sleeve roll.

In this paper, the residual stress for sleeve rolls is mainly discussed toward developing next-generation rolls such as super-cermet rolls. Previously, only the residual stress of the solid roll was discussed as shown in Fig. 11(b) in Section 4.3 through the quenching/tempering

simulation [42–44]. In roll companies, the surface residual stress of the roll is always confirmed after tempering the roll by using non-destructive inspections as described above. The authors' previous simulation may provide the residual stress distribution from the surface to the inside of the roll under various heat treatments. Since the internal stress cannot be obtained by using these non-destructive methods, the destructive inspections such as Sachs boring method and disk cut method were sometimes applied spending high cost and time-consuming effort [58,59]. In this sense, the residual stress simulation has been requested to obtain the residual stress distribution from the surface to the inside of the roll under various heat treatments.

In this paper, the residual stress of the sleeve roll will be investigated by applying the previous analysis method used for the solid roll. Then, both results will have compared to each other. For the readers' convenience, therefore, the outline of the residual stress analysis method of the solid roll is provided in Appendix A.

2.2. Sleeve roll manufacturing process

In this paper, to clarify a suitable manufacturing method for sleeve rolls, two extreme cases indicated in Figs. 2 and 3 will be investigated. Fig. 2 illustrates a manufacturing method named "solid heat treatment" where the solid roll is quenched/tempered. Here, as an extreme case of a large amount of allowance, the solid roll is assumed. This is because the previous results for the solid roll can be used. The second process shown in Fig. 2(c) is lathe boring the inside of the solid roll having the residual stress to manufacture the sleeve. Then, the shaft is shrink-fitted as shown in Fig. 3(d). Since the detail of the heat treatment of the solid roll in Fig. 2(b) was described in the previous paper [42–44], only the outline of the simulation is indicated in Appendix A. The obtained residual stress will be shown later in Figs. 7(a), 11(b), and 12(b).

Fig. 3 illustrates another manufacturing method named "sleeve heat treatment" where the sleeve is quenched/tempered. In Fig. 3, the sleeve with no allowance is assumed as an extreme case of a small amount of allowance. As shown in Fig. 3(b), the first process is boring the solid roll to manufacture the sleeve with no allowance. The second process in Fig. 3(c) is quenching/tempering the sleeve. Then, the shaft is shrink-fitted as shown in Fig. 3(d). The obtained residual stress will be shown later in Figs. 7(b), 11(a), and 12(a).

In the following sections, two extreme cases in Figs. 2 and 3 will be discussed to obtain the suitable residual stress for sleeve rolls. The target compressive residual stress at the outer surface can be in the range $\sigma_\theta = 200 \sim 400$ MPa and the target tensile residual stress at the inner surface can be $\sigma_\theta \leq 200$ MPa. In actual manufacturing, the first process is centrifugal casting to produce an intermediate shape between Figs. 2(b) and 3(b).

The second process is quenching/tempering the sleeve with a certain amount of allowance. The third process is boring the sleeve to remove the allowance remaining at the inner surface for the shaft to shrink-fitted.

2.3. Analytical model and boundary conditions

Fig. 1(a) shows the HSS/DCI solid roll analyzed in the previous paper where the body diameter D = 700 mm with 60 mm outer layer thickness and 1800 mm length [42,43]. The outer layer is made of HSS and the inner layer including the shaft is made of DCI manufactured by centrifugal casting. Figs. 2 and 3 show the detailed dimensions of the bimetallic sleeve roll discussed in this paper. The external shape and dimensions are the same as those of the solid roll in Fig. 1(a). The sleeve has a 125 mm thickness and a 450 mm inner diameter shrink-fitted with a shrink-fitting allowance, δ.

In this study, the MSC Marc 2012 software is applied to FEM thermo-elastic-plastic analysis to simulate the quenching/tempering process. Fig. 4 illustrates the axisymmetric analysis FEM model for solid roll in Fig. 1(a). A 4-node linear axisymmetric quad element with a mesh size of

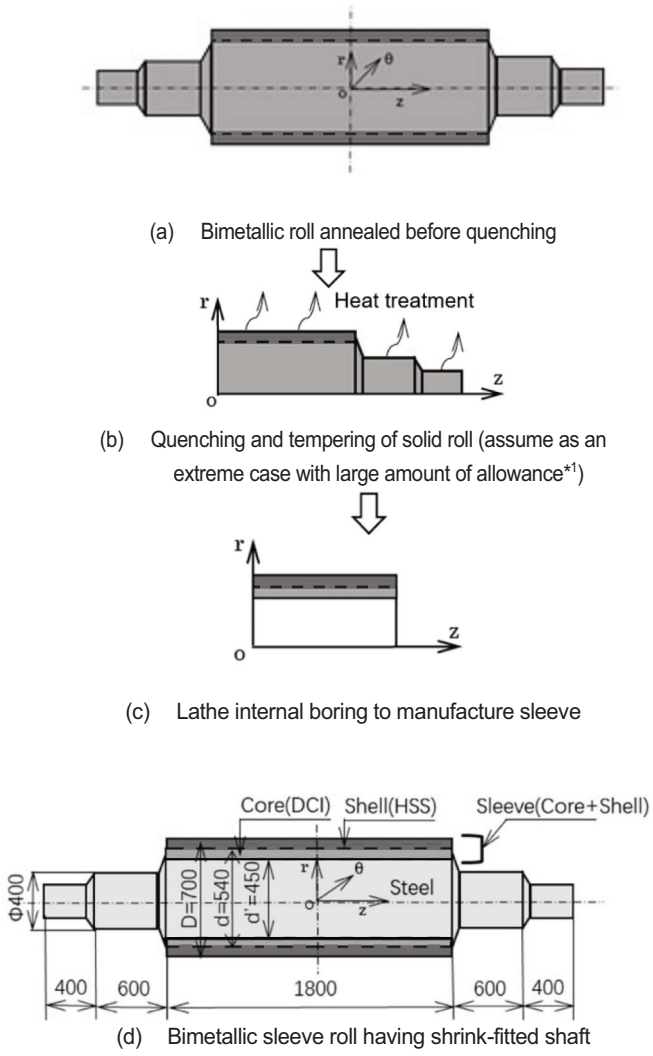

Fig. 2. A manufacturing method named "solid heat treatment" where the solid roll is quenched/tempered.
(a) Bimetallic roll annealed before quenching.
(b) Quenching and tempering of solid roll (assume as an extreme case with large amount of allowance*1).
(c) Lathe internal boring to manufacture sleeve.
(d) Bimetallic sleeve roll having shrink-fitted shaft.
*1: The solid roll in Fig. 2(b) is assumed as an extreme case of a large amount of allowance. In actual manufacturing, the first process is centrifugal casting to produce an intermediate shape between Figs. 2(b) and 3(b). The second process is quenching/tempering the sleeve with a certain amount of allowance. The third process is boring the sleeve to remove the allowance remaining at the inner surface for the shaft to shrink-fitted.

5 mm × 5 mm is adopted for the transient-static simulation. The displacement boundary conditions and thermal isolation conditions are applied to z = 0 due to the symmetry. In this study, the roll surface temperature obtained by measuring experimentally is imposed on the roll surface.

The heat transfer coefficient depends on many factors, such as material, size, and surface conditions of a part. At the beginning of this study, therefore, the heat transfer coefficient was obtained in the following way. First, a value of heat transfer coefficient is assumed from the literature and applied to the FEM roll surface with an ambient temperature. Here, the ambient temperature is obtained by measuring experimentally. Then, the roll surface temperature is obtained by the FEM analysis and compared with the roll surface temperature experimentally obtained. Third, the assumed heat transfer coefficient is

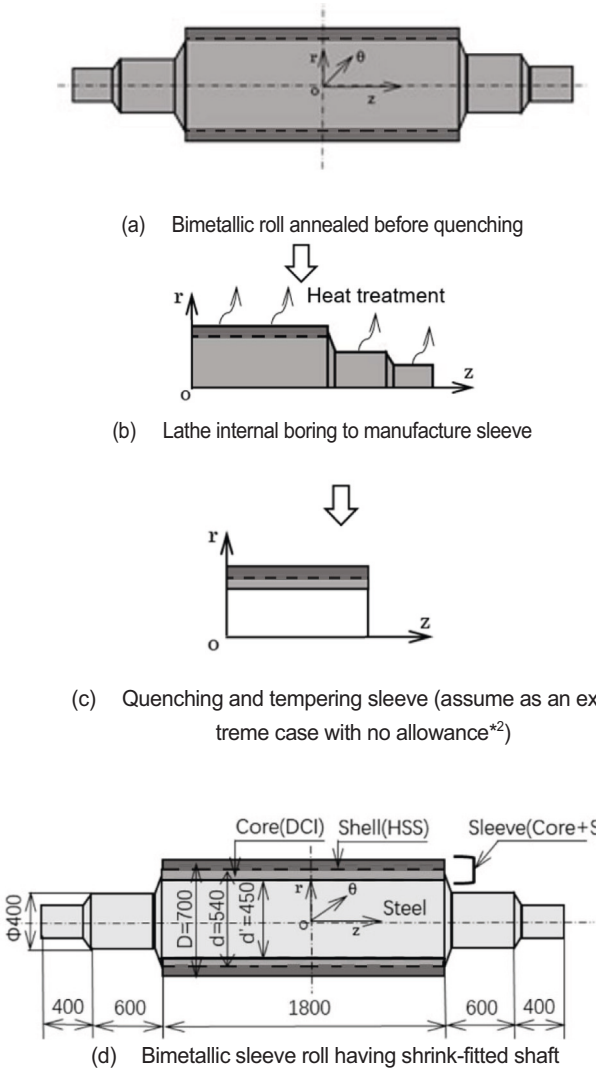

Fig. 3. A manufacturing method named "sleeve heat treatment" where the sleeve is quenched/tempered. The sleeve with no allowance in Fig. 2(c) is assumed as an extreme case of a small amount of allowance.
(a) Bimetallic roll annealed before quenching.
(b) Lathe internal boring to manufacture sleeve.
(c) Quenching and tempering sleeve (assume as an extreme case with no allowance*2).
(d) Bimetallic sleeve roll having shrink-fitted shaft.
*2: The sleeve in Fig. 3(c) is assumed as an extreme case of a small amount of allowance. In actual manufacturing, the first process is centrifugal casting to produce an intermediate shape between Figs. 2(b) and 3(b). The second process is quenching/tempering the sleeve with a certain amount of allowance. The third process is boring the sleeve to remove the allowance remaining at the inner surface for the shaft to shrink-fitted.

changed repeatedly. The real heat transfer coefficient is finally obtained when the simulation temperature coincides with the roll surface temperature. After analyzing the temperature distribution, thermal stress distribution can be obtained from standard thermo-elastic-plastic FEM analysis.

In this study, the effect of the creep on the residual stress is considered when the temperature is kept constant during the heat treatment (see T_{Keep} period in Fig. 9 and tempering period in Fig. 10 in Section 4). As shown in the previous paper [43], the creep test was conducted by using the specimen prepared from the DCI layer to obtain the creep Eqs. (1) and (2) in Section 4. To confirm the validity of those equations, the stress relaxation test was also conducted. Through this stress reduction

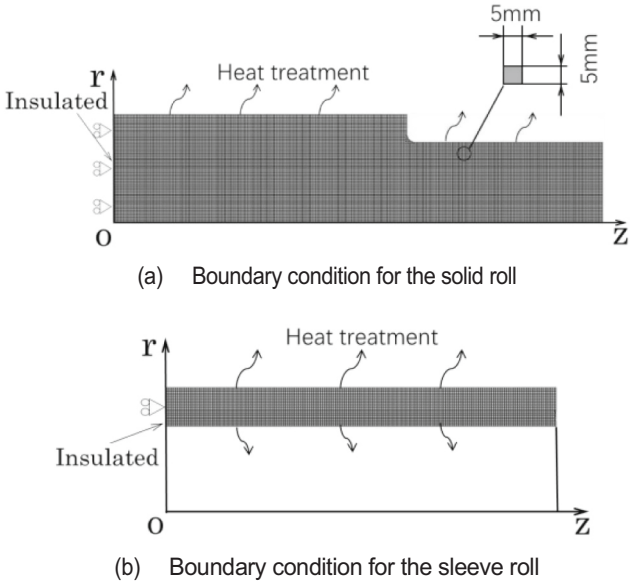

Fig. 4. Boundary condition for the solid roll and the sleeve roll.
(a) Boundary condition for the solid roll.
(b) Boundary condition for the sleeve roll

coincidence, the FEM analysis incorporated with those equations was found to be useful for predicting the creep effect on the residual stress.

2.4. Mechanical properties of outer and inner layer materials

Fig. 5 shows the microstructure around the HSS/DCI boundary [27,44]. The fine carbides with white color are uniformly distributed on the outer HSS layer side. However, toward the internal DCI layer side, coarse carbides can be seen. In the inner layer DCI, the spherical graphite surrounded by the ferrite is distributed uniformly around the boundary showing a healthy composite structure. Table 1 shows the material properties of the outer HSS layer and the inner DCI layer at room temperature including the effects of phase transformation. The properties at high temperatures used in this simulation are obtained experimentally by using the specimen cut-out from the roll manufactured in the same way.

Fig. 6 shows several material properties including stress-strain curves, Poisson's ratio, Young's modulus, specific heat, thermal expansion coefficient, and thermal conductivity from 23 °C to 1000 °C for HSS and DSI. The results in Fig. 6 are obtained by using simulation software which calculates a wide range of materials properties for alloys and is particularly aimed at multi-component alloys used in industrial practice [61]. This is partly because roll manufacturing companies cannot expose the details of the mechanical properties of the rolls they manufactured.

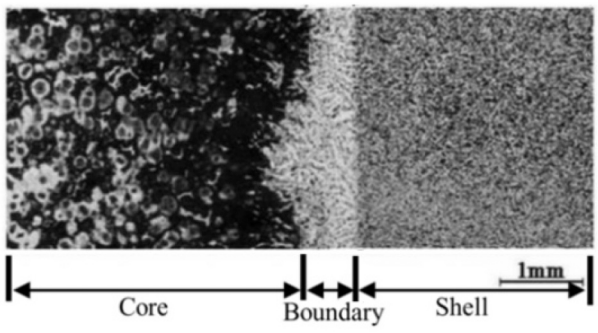

Fig. 5. Microstructure around HSS/DCI boundary [15–17].

Table 1
Mechanical properties of HSS and DCI at room temperature.

Property	HSS	DCI
Tensile strength, σ_B (MPa)	1570	415
Fatigue strength*3, σ_{w0} (MPa)	630	166
Yield Strength (MPa)	1270	410
Young's modulus (GPa)	233	173
Poisson's ratio	0.3	0.3
Density (kg • m^3)	7600	7300
Thermal expansion coefficient (K^{-1})	12.6×10^{-6}	13.0×10^{-6}
Thermal conductivity (W/mK)	20.2	23.4
Specific heat (J/kgK)	0.46	0.46

*3: Estimated from Fatigue strengt/Tensile strength = σ_{w0}/σ_B=0.4 [60].

3. Residual stress distribution of bimetallic roll

3.1. Residual stress due to solid heat treatment

Fig. 7 illustrates the residual stress due to the solid heat treatment in Fig. 2. First, consider the bimetallic solid roll in Fig. 2(a). Then, the residual stress due to quenching/tempering in Fig. 2(b) was analyzed based on the previous studies [42–44] (see Fig. 11(b) in later Section 4.3). Then, Fig. 7(a) is the results of the sleeve in Fig. 2(c), which is obtained through lathe boring the quenched/tempered solid roll. Fig. 7 (b) is the result for Fig. 2(d), which is obtained through shrink-fitting the shaft into the sleeve manufactured in Fig. 2(c).

Fig. 7(a) shows the stress distribution σ_θ at cross-section z = 0, where the maximum tensile stress $\sigma_\theta = 463$ MPa appears at $r = 270$ mm. Other cross sections $z \neq 0$ are also investigated, and it is found that $\sigma_\theta = 463$ MPa is the largest. The residual stress in the inner layer at z = 0 is in the range $\sigma_\theta = 453 \sim 463$ MPa exceeding the tensile strength of DCI $\sigma_\theta = 415$ MPa. As shown in Fig. 7(b) showing the residual stress distribution after shrink-fitting the shaft, the maximum tensile stress increases to $\sigma_\theta = 514$ MPa at $r = 225$ mm.

3.2. Residual stress due to sleeve heat treatment

Fig. 8 illustrates the residual stress due to the sleeve heat treatment in Fig. 3. In this case, assume that from the bimetallic solid roll in Fig. 3(a) the sleeve in Fig. 3(b) is manufactured through lathe boring. Then, Fig. 8 (a) is the result in Fig. 3(c) obtained through quenching/tempering the sleeve in Fig. 3(b). Fig. 8(b) is the result for Fig. 3(d) obtained through shrink-fitting the shaft into the sleeve quenched/tempered in Fig. 3(c).

Fig. 8(a) shows the stress distribution σ_θ at cross-section z = 0, where the maximum tensile stress $\sigma_\theta = 95$ MPa appears at $r = 225$ mm. Other cross sections $z \neq 0$ are also investigated, and it is found that $\sigma_\theta = 95$ MPa is the largest and the compressive stress $\sigma_\theta = 333$ MPa at (r, z) = (270, 0) is not the largest. Therefore, the residual stress distribution σ_θ at z = 0 can be used to discuss the validity of sleeve heat treatment since smaller tensile stress and larger compressive stress are desirable.

The maximum tensile stress $\sigma_\theta = 95$ MPa in Fig. 8(a) is much smaller than the maximum stress in Fig. 7(a) and also much smaller than the tensile strength of DCI. Also, the compressive residual stress $\sigma_\theta = 333$ MPa at the outer surface is large enough to prevent the fatigue crack extension. It can be concluded that the sleeve heat treatment type as shown in Fig. 3 is useful for manufacturing the sleeve roll.

Fig. 8(b) shows the residual stress distribution after shrink-fitting the shaft, where the maximum tensile stress $\sigma_\theta = 156$ MPa at r = 225 mm is small enough. Furthermore, the maximum compressive stress $\sigma_\theta = 297$ MPa at $r = 270$ mm is still large enough.

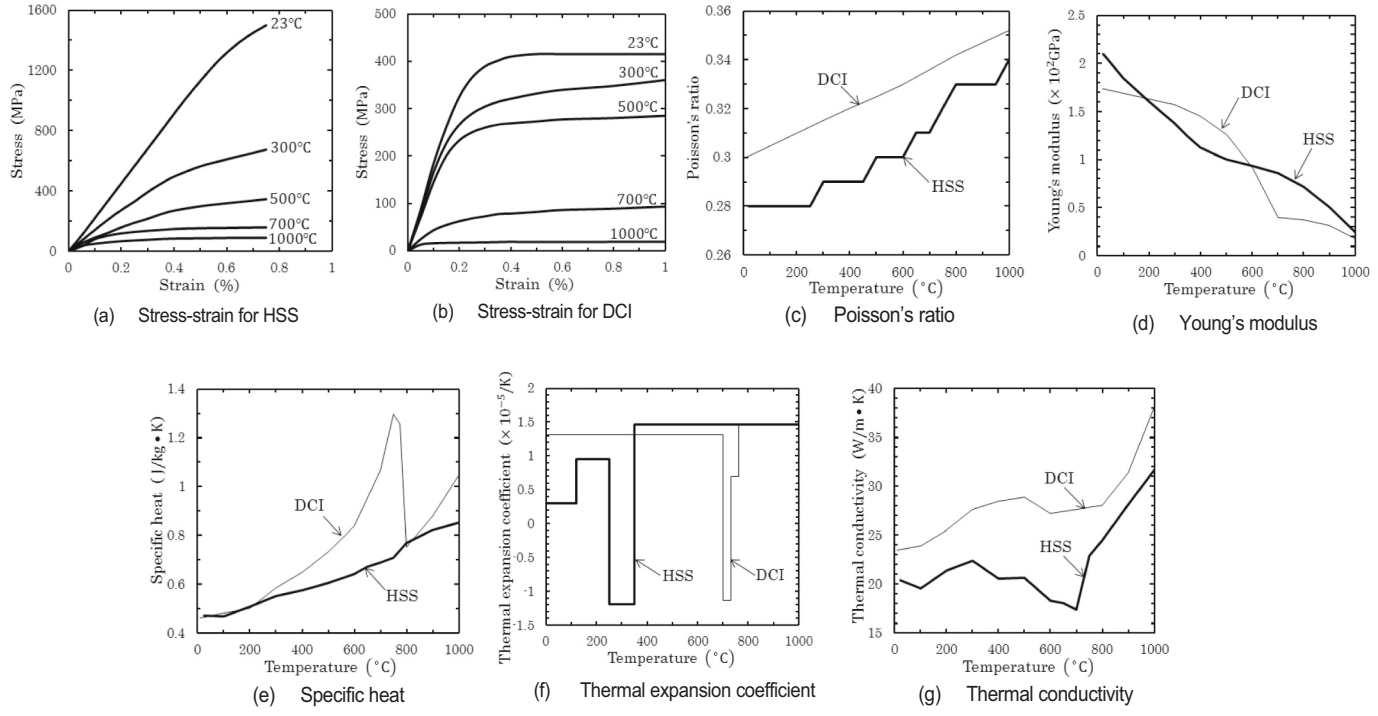

Fig. 6. Material properties for both HSS and DCI.
(a) Stress-strain for HSS.
(b) Stress-strain for DCI.
(c) Poisson's ratio.
(d) Young's modulus.
(e) Specific heat.
(f) Thermal expansion coefficient.
(g) Thermal conductivity.

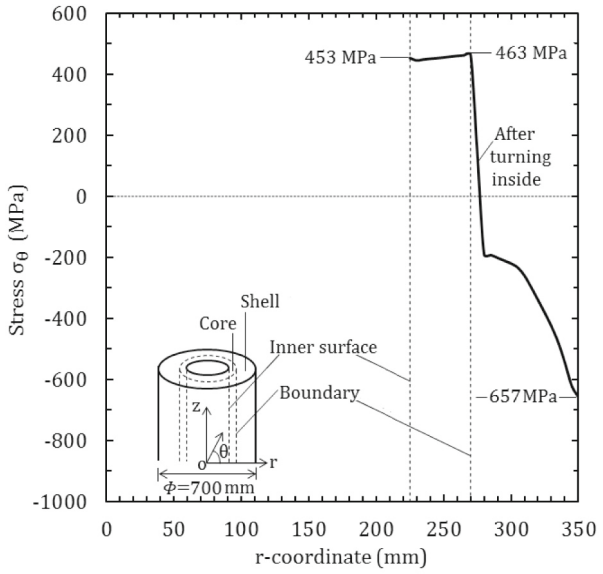

(a) Residual stress σ_θ distribution before shrink-fitting in Fig. 2(c)

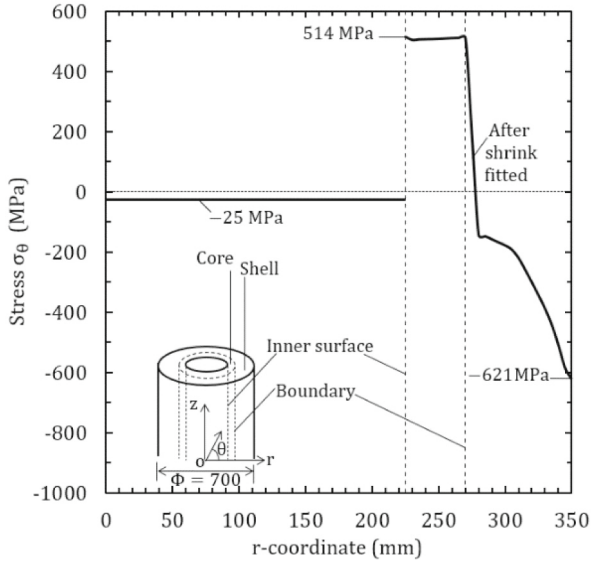

(b) Residual stress σ_θ distribution after shrink-fitting in Fig. 2(d)

Fig. 7. Residual stress σ_θ distribution at z = 0 (solid heat treatment).
(a) Residual stress σ_θ distribution before shrink-fitting in Fig. 2(c).
(b) Residual stress σ_θ distribution after shrink-fitting in Fig. 2(d).

3.3. *Comparison of the residual stress of bimetallic roll for both manufacturing methods*

The above discussion clarified that the tensile residual stress in Fig. 8 (a) is smaller than the tensile residual stress in Fig. 7(a). In the solid heat treatment method, the tensile stress appears widely in the solid roll inside (see Fig. 11(b) in Section 4.4). Then, boring the solid roll inside increases the tensile stress of the inner layer due to the reduction of the cross-sectional area. Instead, in the sleeve heat treatment method, due to the heat treatment to the sleeve already manufactured, the tensile residual stress at the inner sleeve surface is relatively smaller. It can be concluded that the sleeve heat treatment in Fig. 3 is suitable for manufacturing sleeve rolls since the maximum tensile residual stress σ_θ = 95 MPa is small and the compressive stress at the outer surface σ_θ = 333 MPa is large enough.

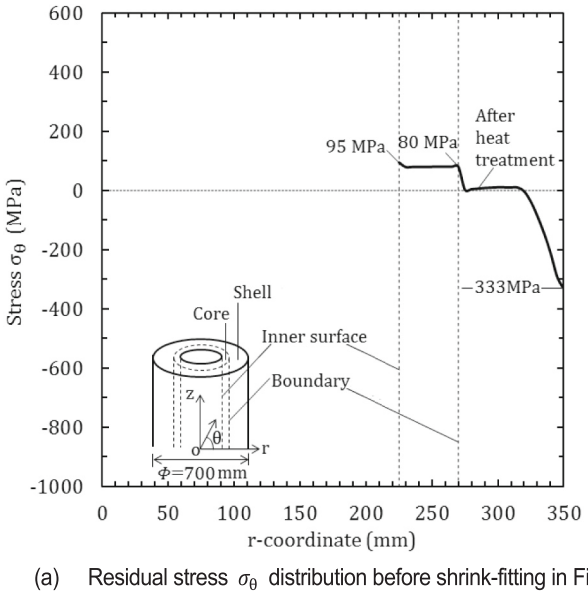

(a) Residual stress σ_θ distribution before shrink-fitting in Fig. 3(c)

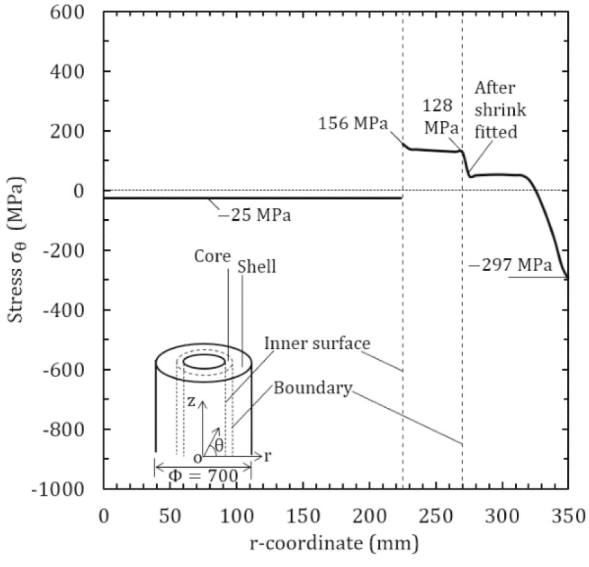

(b) Residual stress σ_θ distribution after shrink-fitting in Fig. 3(d)

Fig. 8. Residual stress σ_θ distribution at z = 0 (sleeve heat treatment).
(a) Residual stress σ_θ distribution before shrink-fitting in Fig. 3(c).
(b) Residual stress σ_θ distribution after shrink-fitting in Fig. 3(d).

4. Residual stress generation mechanism for the bimetallic sleeve roll

The above sections clarified that the sleeve heat treatment illustrated in Fig. 3 is suitable for manufacturing sleeve rolls. In the previous studies, the residual stress generation mechanism was discussed for the bimetallic sleeve roll. In this Section 4, the residual stress generation mechanism will be discussed for the bimetallic sleeve roll in Fig. 3(c) to clarify why the residual stress becomes smaller. The simulations are based on the analytical model and boundary conditions shown in Fig. 4 (b) in Section 2.3. In Appendix A, the outline of the residual stress generation is indicated for the bimetallic solid roll in Fig. 2(b) since the detail was discussed in the previous papers [42–44].

4.1. *Temperature and stress change during the quenching*

In this section, the residual stress during quenching is analyzed and

the residual stress generation mechanism is discussed. Fig. 9(a) illustrates the temperature history during the heating process in Region I and the quenching process in Region II and Region III. Fig. 9(b) illustrates the corresponding stress, σ_θ for Region I, Region II, and Region III. The temperature and the stress, σ_θ during the process in Region I to Region III can be explained in the following way.

In Region I: The temperature is almost the same as the quenching temperature T_{Start} in the whole sleeve with a small temperature difference maintained. The stress during pre-heating before quenching can be ignored.

In Region II: Due to quenching, the outer sleeve surface is cooled down from the temperature T_{Start}. Then, initially, the tensile stress at the surface appears and increases due to the shrinkage of the outer layer, but this tensile stress immediately changes to the compressive stress.

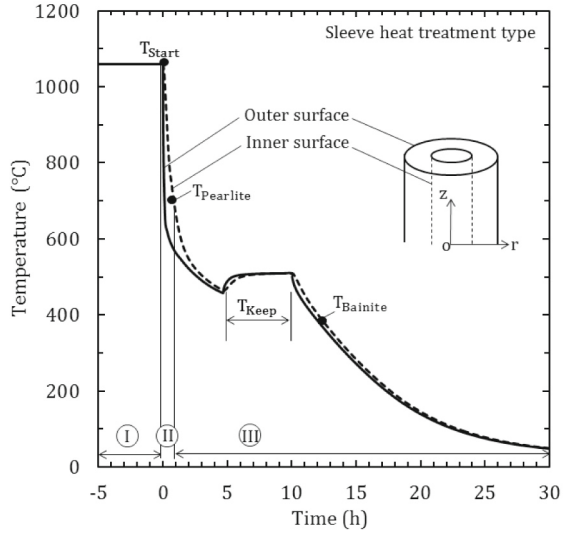

(a) Temperature at inner and outer surfaces provided along $|z| \leq 900$ mm in Fig. 3(c)

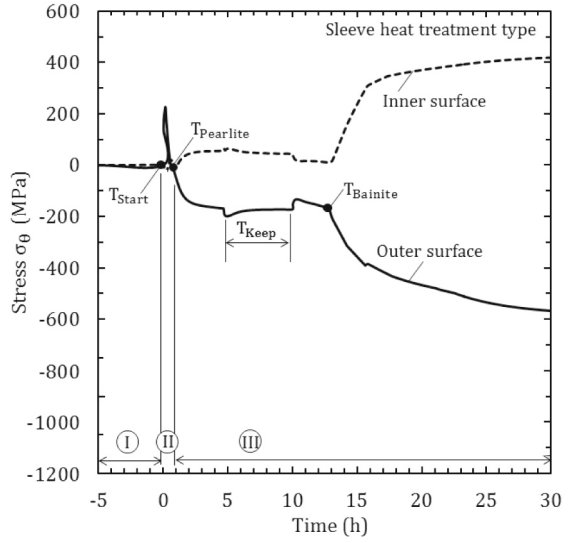

(b) Stress σ_θ at inner and outer surfaces when $z = 0$ in Fig. 3(c)

Fig. 9. Temperature and σ_θ histories in sleeve heat treatment during quenching in Fig. 3(c).
(a) Temperature at inner and outer surfaces provided along $|z| \leq 900$ mm in Fig. 3(c).
(b) Stress σ_θ at inner and outer surfaces when $z = 0$ in Fig. 3(c).

This is because the thermal shrinkage at the inner sleeve portion becomes larger than the thermal shrinkage at the outer sleeve surface. Therefore the plastically elongated outer sleeve surface needs compression. At $T_{Pearlite}$, the pearlite expansion transformation appears at the inner layer. During this process, starting from the HSS/DCI boundary toward the inside surface, the compressive stress at the inner surface decreases until $T_{Pearlite}$ occurs. Then the stress at the inner surface center and the stress at the outer surface intersect.

In Region III: The residual stress of the outer layer rapidly changes to the compression due to the pearlite transformation expansion at the inside sleeve portion. Then, the tensile stress at the center increases due to the higher cooling rate. The stress at the inner layer becomes tensile, and the stress at the outer layer stress becomes compressive.

When the temperature becomes T_{Keep} (keeping temperature period), the temperature is maintained by heating up the outer surface to adjust the initial excessive cooling. During this T_{Keep}, the compressive and tensile stresses increase slightly, and after that, the temperature difference disappears and the internal and external stresses decrease slightly. When the surface cooling starts again after T_{Keep} the bainite transformation expansion occurs in the outer layer at the temperature $T_{Bainite}$, and the compressive stress increases. The tensile stress at the inner surface also increases to balance the outer layer's compressive stress. In the cooling process after bainite transformation, the tensile stress increases due to the shrinkage at the inner layer, and to balance this the compressive stress at the outer layer increases. At the end of quenching, the residual stress at the inner surface becomes 418 MPa.

4.2. Temperature and stress change during the tempering

Tempering treatment reduces the excessive residual stress due to quenching. Tempering also promotes the martensitic transformation of retained austenite in the microstructure. The previous studies indicated that the stress reduction due to tempering is mainly caused by the creep effect [62]. In this study, therefore, the time hardening law called a power law is used to express the creep behavior of the inner material DCI having lower strength under high temperature [42]. Eq. (1) is the creep constitutive equation of the inner layer DCI at the time t [63].

$$\varepsilon_c = A\sigma^m t^n \tag{1}$$

The creep experimental was conducted under the constant stresses $\sigma = 130$ MPa and $\sigma = 160$ MPa at T_{Keep}. Then, the constants A, m and n in Eq. (1) were determined and the following Eq. (2) was obtained [64–66].

$$\varepsilon_c = 8.43 \times 10^{-16}\sigma^{5.003}t^{0.4919} \tag{2}$$

Fig. 10 shows the temperature history after tempering at the outer and inner surfaces in Fig. 3(c) and the corresponding stress change σ_θ. As a result of twice tempering, the residual stress at the inner surface is significantly reduced to $\sigma_\theta = 94$ MPa, which is 22 % of the stress at the end of quenching.

4.3. Stress reduction due to tempering expressed in terms of σ_θ and Mises stress σ_{eq}

The reason why the residual stress reduction is larger in the sleeve heat treatment will be discussed in comparison with the stress reduction in the solid heat treatment. Fig. 11(a) and (b) show the residual stress distributions σ_θ in the sleeve heat treatment type in Fig. 3(c) and in the solid heat treatment type in Fig. 2(b). Here, the results are indicated at the beginning of the first tempering, at the beginning of the second tempering, and at the end of the second tempering. The sleeve roll result focuses on the stress at the inner surface $r = 225$ mm, while the solid roll result focuses on the stress at the center $r = 0$ as a representative point of the inner layer. Then, the larger stress reduction effect in the first tempering process is discussed.

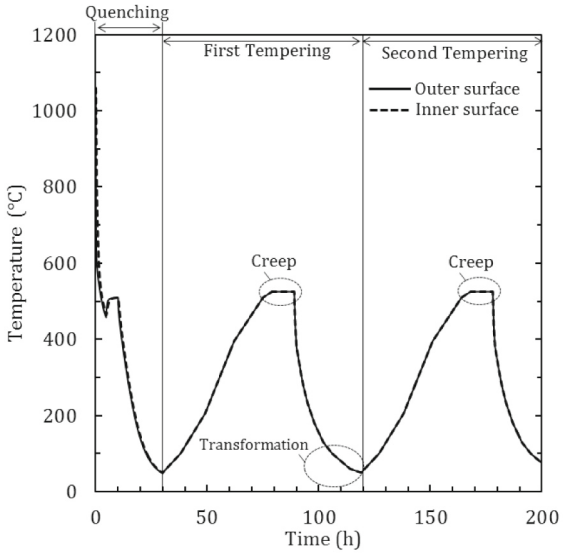

(a) Temperature at inner and outer surfaces provided along $|z| \leq 900$ mm in Fig. 3(c)

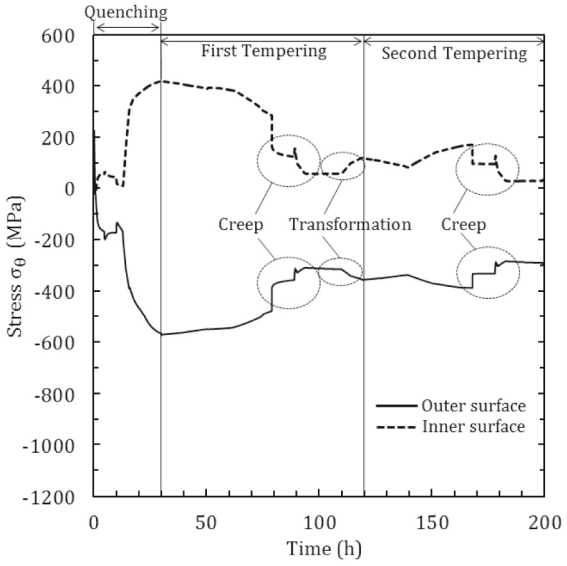

(b) Stress σ_θ at inner and outer surfaces when $z = 0$ in Fig. 3(c)

Fig. 10. Temperature and σ_θ histories in sleeve heat treatment in Fig. 3(c).
(a) Temperature at inner and outer surfaces provided along $|z| \leq 900$ mm in Fig. 3(c).
(b) Stress σ_θ at inner and outer surfaces when $z = 0$ in Fig. 3(c).

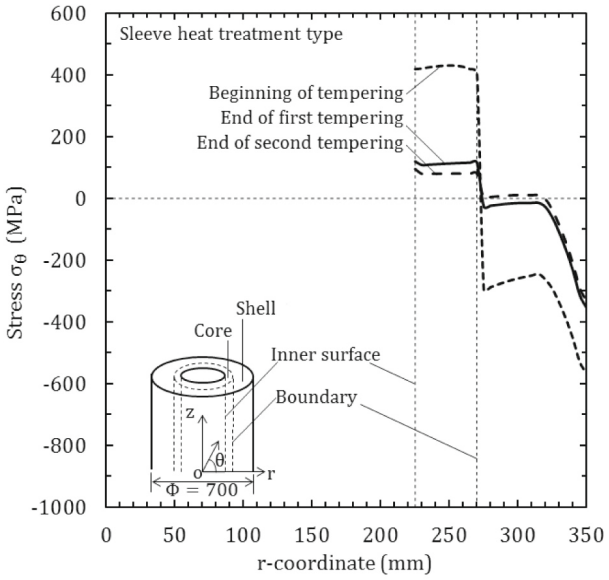

(a) Residual stress σ_θ at $z = 0$ in Fig. 3(c)

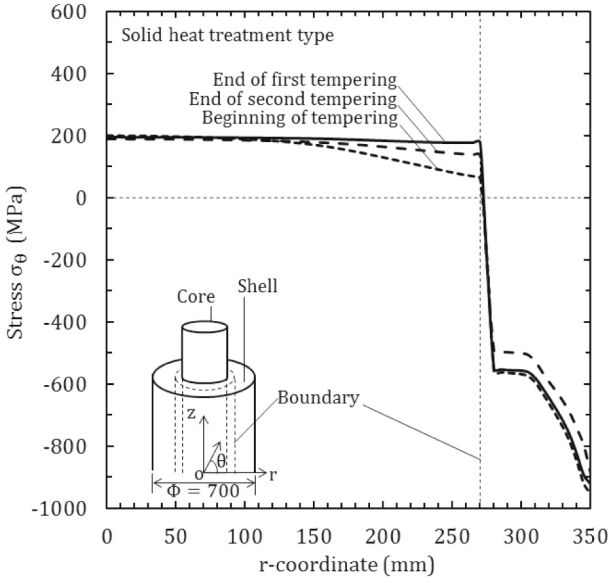

(b) Residual stress σ_θ at $z = 0$ in Fig. 2(b)

Fig. 11. Comparison of stress distribution at $z = 0$ between Figs. 3(c) and 2(b).
(a) Residual stress σ_θ at $z = 0$ in Fig. 3(c)
(b) Residual stress σ_θ at $z = 0$ in Fig. 2(b).

By comparing Fig. 11(a) and (b), the inner surface stress at the beginning of the tempering 418 MPa in the sleeve heat treatment (Fig. 3 (c)) is about twice larger than the stress in the solid heat treatment (Fig. 2(b)). However, at the end of tempering, the sleeve heat treatment type (Fig. 3(c)) has smaller residual stress at the inner surface. As shown in Fig. 11(a), σ_θ at the inner surface ($r = 225$ mm) of the sleeve roll is reduced by 71 % after the first tempering process. However, σ_θ at the center ($r = 0$) of the solid roll (Fig. 11(b)) is reduced by about 2 % after the first tempering process. In this way, the sleeve heat treatment has a remarkable stress reduction at the inner surface residual stress σ_θ by the tempering process compared to the solid heat treatment type.

Next, the equivalent von Mises stress σ_{eq} is considered to discuss the stress reduction effect. Under multiaxial stress, the equivalent von Mises stress σ_{eq} can be regarded as the driving stress of creep deformation instead of the uniaxial stress σ in the creep constitutive Eq. (2) [66,67]. Here, the inner layer stress at $r = 225$ mm in the solid roll is compared with the inner surface stress at $r = 225$ mm in the sleeve roll. In other words, the creep effect is discussed by substituting the equivalent von Mises stress σ_{eq} to the stress σ in Eq. (2).

Fig. 12(a) shows the residual distributions of Von Mises stress σ_{eq} controlling the creep in the sleeve heat treatment after each heat treatment. Fig. 12(b) shows the results in the solid heat treatment type.

From Fig. 12, the larger stress reduction of σ_{eq} is seen in the sleeve heat treatment compared to the solid heat treatment type. This is similar to the stress reduction of σ_θ in Fig. 11. The Von Mises stress at the inner surface $r = 225$ mm in the sleeve roll at the initial stage of tempering $\sigma_{eq} = 407$ MPa is more than twice larger than the one of the solid heat

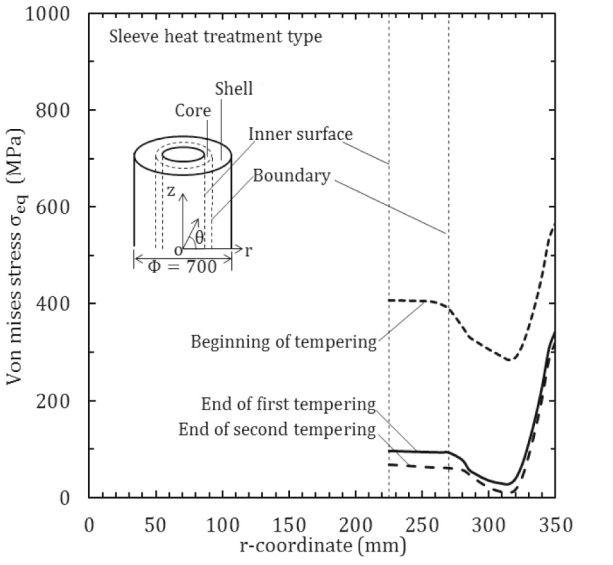

(a) Equivalent von Mises stress σ_{eq} at z = 0 in Fig. 3(c)

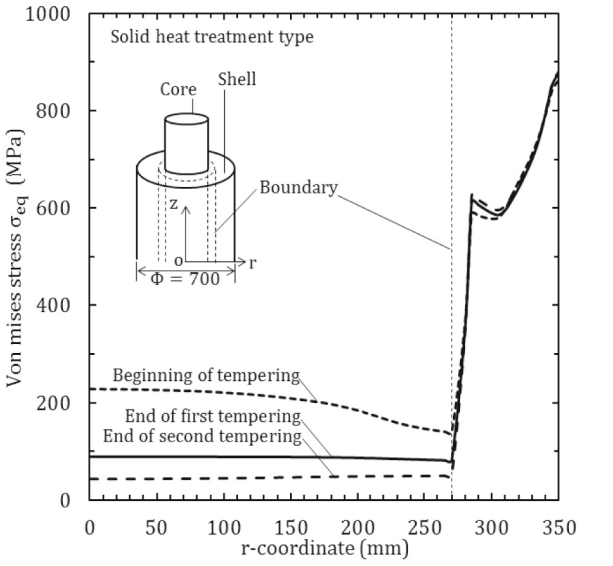

(b) Equivalent von Mises stress σ_{eq} at z = 0 in Fig. 2(b)

Fig. 12. Comparison of equivalent von Mises stress σ_{eq} at z = 0 between Figs. 3(c) and 2(b).
(a) Equivalent von Mises stress σ_{eq} at z = 0 in Fig. 3(c)
(b) Equivalent von Mises stress σ_{eq} at z = 0 in Fig. 2(b).

treatment σ_{eq} = 163 MPa. This is because in the sleeve heat treatment the inner surface is stress-free, while in the solid heat treatment type the stress state is triaxial.

5. Fatigue risk evaluation for bimetallic solid roll and bimetallic sleeve roll constructed by shrink-fitting

Table 2 and Table 3 show the maximum stress, minimum stress, mean stress, and stress amplitude at r = 225 mm and at r = 270 mm. These critical regions are considered based on the previous roll failures experienced in industries [24], where the critical region for the bimetallic solid roll is near the HSS/DCI boundary (r = 270 mm) and the critical region for the bimetallic sleeve roll is at the shrink-fitted region (r = 225 mm). Also, previous studies explained the roll failure near the boundary HSS/DCI inside of the bimetallic solid roll is caused by the variation of σ_r during the roll rotation. And the slip failure at the shrink-fitted region inside of the bimetallic sleeve roll is caused by the variation of σ_θ. Therefore, the maximum and minimum values of σ_θ and σ_r at r = 225 mm and r = 270 mm during a roll rotation can be the driving force causing the internal failure for both bimetallic solid roll and bimetallic sleeve roll.

Table 2
Maximum stress, minimum stress, mean stress, stress amplitude at r = 225 mm.

Stress	σ_{max} (MPa)	σ_{min} (MPa)	σ_m (MPa)	σ_a (MPa)	$\sigma_m + \sigma_{res}$ (MPa)
σ_θ^{solid}	8	−56	−24	32	130
σ_r^{solid}	10	−299	−145	155	14
σ_θ^{sleeve}	91	−25	33	58	189
σ_r^{sleeve}	2	−140	−69	71	−94

Table 3
Maximum stress, minimum stress, mean stress, stress amplitude at r = 270 mm.

Stress	σ_{max} (MPa)	σ_{min} (MPa)	σ_m (MPa)	σ_a (MPa)	$\sigma_m + \sigma_{res}$ (MPa)
σ_θ^{solid}	9	−133	−62	71	74
σ_r^{solid}	7	−453	−223	230	−77
σ_θ^{sleeve}	105	−9	48	57	176
σ_r^{sleeve}	−1	−167	−84	83	−96

In this section, although the standard rolling force ratio is P/P_{total} = 1.0, a more severe rolling force ratio P/P_{total} = 1.5 is considered to evaluate fatigue failure risk because the rolling trouble may cause such impact force due to the rolling plate biting and the temperature drop of the rolled material. In Table 2 and Table 3, the superscript "solid" represents the bimetallic solid roll while the superscript "sleeve" represents the bimetallic sleeve roll. Table 2 and Table 3 also show the mean stress $\sigma_m + \sigma_{res}$ which represents the superposing of the mean stress σ_m with the residual stress σ_{res}. Residual stress for the bimetallic solid roll is taken from the previous study [62]. Meanwhile, for the bimetallic sleeve roll, the residual stress is considered in Fig. 8(b).

Since the mean stress in Table 2 and Table 3 for the bimetallic solid roll is large compressive stress, the fatigue limit lines should be newly prescribed under large compressive stress since no study is available. Fatigue failure under large compressive stress was treated by several previous papers but usually, they considered rolling contact fatigue in ball/roller bearings and backup roll surface spalling [68,69]. Only a few data are available for ordinary fatigue strength under large compressive stress fields [70].

Fig. 13 shows a stress amplitude versus mean stress diagram (σ_a-σ_m diagram) to discuss the fatigue limit for the stresses in Table 2 and Table 3. The thick solid lines passing through points A, D, F, G, and H in Fig. 13 determines the fatigue limit line. Details of this fatigue limit line A-D-F-G-H is included in Appendix B [71]. Fig. 13(a) shows the fatigue limit diagram at r = 225 mm and Fig. 13(b) shows the fatigue limit diagram at r = 270 mm. Fig. 13(a) and (b) shows the change of the mean stress σ_m after superposing the residual stress σ_{res}. All stresses move closer to the fatigue limit line due to the tensile residual stress except σ_r^{sleeve} for the bimetallic sleeve roll due to the compressive residual stress.

Table 4 shows the safety factor evaluation for the stresses in Fig. 13. The safety factor is defined as $SF = \overline{OB'}/\overline{OB}$ where O is the origin point, B is the stress point, and B′ is the intersection point of line OB to the fatigue limit line (see Fig. B.1). A larger SF value means the point is relatively safer than another point having a smaller SF value. Therefore, the relative safety factor SF can be used to compare the risk of fatigue failure. At r = 270 mm, the most dangerous stress for the bimetallic solid roll can be found as σ_r^{solid} with SF = 0.94 and the most dangerous stress for the bimetallic sleeve roll can be found as σ_θ^{sleeve} with SF = 1.30. Similar results are obtained at r = 225 mm and can be expressed as σ_r^{solid}

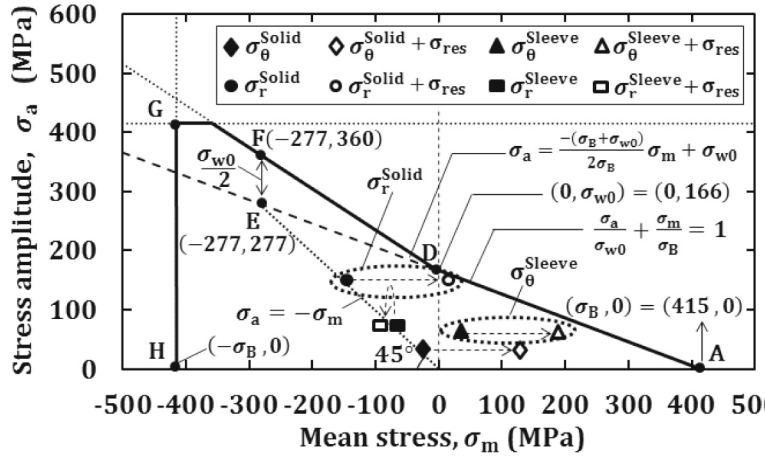

(a) Fatigue limit diagram evaluation at shrink-fitted portion r=225 mm for both sleeve and solid rolls

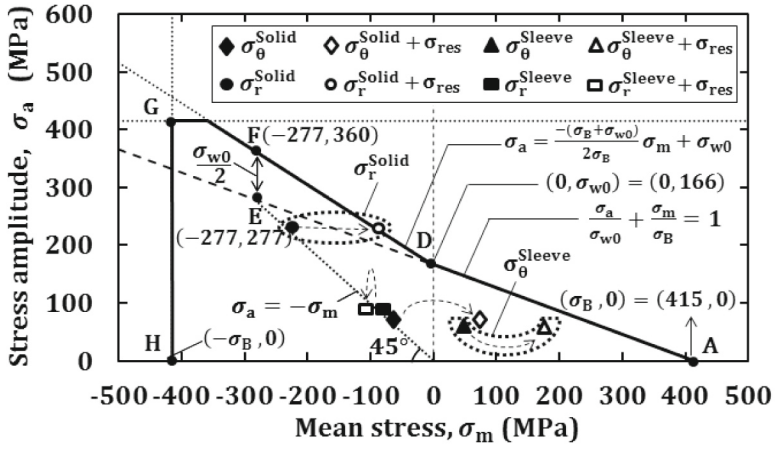

(b) Fatigue limit diagram evaluation at HSS/DCI boundary r=270 mm for both sleeve and solid rolls

Fig. 13. Stress amplitude σ_a versus mean stress σ_m diagram (σ_a - σ_m diagram) for the fatigue limit $\sigma_{w0} = 110$ MPa, and the tensile strength $\sigma_B = 415$ MPa focusing on the stress at $r = 225$ mm and $r = 270$ mm. Notations σ_r^{solid} and σ_θ^{solid} represent the results of the bimetallic solid roll while notations σ_r^{sleeve} and σ_θ^{sleeve} represent the bimetallic sleeve roll. Notation $\sigma_m + \sigma_{res}$ represents the superposing the mean stress σ_m with the residual stress σ_{res}.
(a) Fatigue limit diagram evaluation at shrink-fitted portion r = 225 mm for both sleeve and solid rolls.
(b) Fatigue limit diagram evaluation at HSS/DCI boundary r = 270 mm for both sleeve and solid rolls.

Table 4
Safety factor to evaluate the stresses in Fig. 13.

At r = 225 mm		At r = 270 mm	
Stress	Safety factor	Stress	Safety factor
σ_θ^{solid}	1.98	σ_θ^{solid}	1.65
σ_r^{solid}	1.03	σ_r^{solid}	0.94
σ_θ^{sleeve}	1.24	σ_θ^{sleeve}	1.30
σ_r^{sleeve}	4.41	σ_r^{sleeve}	4.32

with SF = 1.03 and σ_θ^{sleeve} with SF = 1.24. It is found that the stress appearing at the inside of the bimetallic sleeve roll is safer than the stress appearing at the solid bimetallic roll although the damage and defects when the slippage occurs are not taken into consideration yet in this analysis. In recent studies [41,72], the slip defect geometries were identified [41] and the fatigue strength reduction due to the slip defect was discussed [72]. It may be concluded that if such slip defect can be prevented in a proper way such as providing a suitable key, the fatigue strength of the sleeve roll can be improved and comparable to the fatigue strength of the solid roll.

6. Conclusions

Next-generation rolling rolls such as super-cermet rolls can be manufactured only by adopting a sleeve roll structure where the shaft is shrink-fitted into the sleeve. To prevent sleeve cracking due to sleeve slip, reducing the residual stress at the inner surface of the sleeve is important. In this paper, therefore, two extreme manufacturing processes were investigated. One is named “solid heat treatment”, which is the process of quenching/tempering a solid roll and boring the inside to manufacture a sleeve. The other is named “sleeve heat treatment”, which is the process by which the inside of a solid roll is lathed to manufacture a sleeve, which is then quenched/tempered. After a suitable manufacturing method is clarified, the fatigue risk of the sleeve will be discussed in comparison with the results of the solid bimetallic roll in Fig. 1(a). After a suitable manufacturing method is found, the fatigue risk of the sleeve was discussed based on the residual stress and rolling stress. The conclusions can be summarized as follows.

1. The tensile residual stress at the inner surface of the sleeve heat treatment in Fig. 3(c) is much smaller than the tensile residual stress at the inner layer of the solid heat treatment in Fig. 2(c). It may be concluded that the sleeve heat treatment process in Fig. 3 is suitable for manufacturing the sleeve roll since the inner layer of the fracture hardly occurs (see Figs. 7, 8).

2. The tensile residual stress of the sleeve heat treatment in Fig. 3(c) can be reduced significantly by the tempering. This is because the inner surface is free of stress in the sleeve heat treatment although the center of the solid heat treatment in Fig. 2(c) has a triaxiality of stress (see Fig. 12).
3. The fatigue failure risk was investigated by using the fatigue limit diagram with the safety factor SF (see Fig. 13). It may be concluded that if such slip defect can be prevented in a proper way such as by providing a suitable key, the fatigue strength of the sleeve roll can be improved and comparable to the fatigue strength of the solid roll.

Funding

This research did not receive any specific grant from funding agencies in the public, commercial, or not-for-profit sectors.

CRediT authorship contribution statement

Mohd Radzi Aridi: Investigation, Writing original draft. Rahimah Abdul Rafar: Software, Analysis. Nao-Aki Noda: Supervision, Writing final version. Zifeng Sun: Software, Analysis. Yoshikazu Sano: Conceptualization, Review, Advisor. Kakeru Takata: Software, Investigation. Yasushi Takase: Administration, Editing.

All authors have approved of the final article.

Declaration of competing interest

The author declare that they have no known competing financial interests or personal relationships that could have appeared to influence the work reported in this paper.

Appendix A. Residual stress simulation of the bimetallic solid roll

In this paper, Sections 3 and 4 treated the residual stress of the bimetallic sleeve roll newly analyzed. The previous papers [42–44] described the residual stress of the bimetallic solid similarly. For the readers' convenience, this Appendix A will describe the outline of solid stress residual stress analysis previously discussed.

Fig. A.1 illustrates the surface temperature history of the bimetallic solid roll (see Fig. 2(b)) during heat treatment consisting of the pre-heating, quenching, and tempering. In pre-heating process, the whole roll is heated up to the uniform temperature of $T_{Start} = 1050°C$ and kept for several hours. Then, the roll temperature drops rapidly through air cooling. After that, the roll is put into the furnace again and maintained at $T_{Q,Keep}$ to prevent excessive thermal stresses caused by rapid cooling. After keeping period, the roll is cooled down slowly until to the temperature of $T_{T,Finish}$.

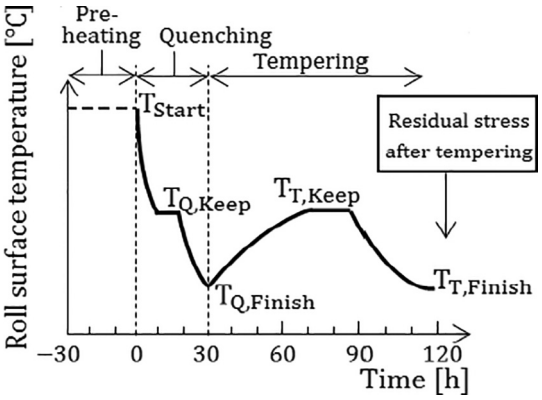

Fig. A.1. Roll surface temperature during heating treatment.

After the quenching process, the tempering process will be performed 2 times to release the residual stress and obtained the stable microstructure. Fig. A.2 shows the histories of (a) temperature and (b) stress σ_z for the bimetallic solid roll during quenching process. The temperature and the stress in Region 1 to Region III have been explained in the Section 4.1 in this paper.

Fig. A.3(a) and (b) show the obtained stress distributions σ_θ, σ_z, σ_r,τ_{rz} and σ_{eq} at $z = 0$. Fig. A.3(a) shows the stress distributions before the first tempering and Fig. A.3(b) shows the ones after the second tempering. From Fig. A.3, it is seen that tempering does not affect σ_r and τ_{rz} very much. Instead, tempering reduces σ_z largely at both inner and outer layers while tempering reduces σ_θ only at the outer layer.

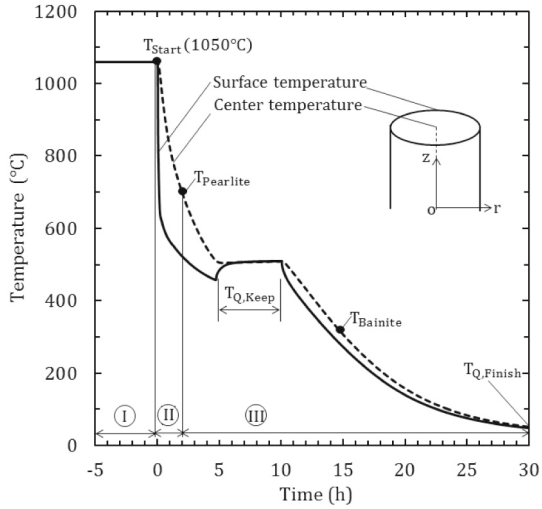

(a) Temperature at inner and outer surface along $|z| \leq 900$ mm

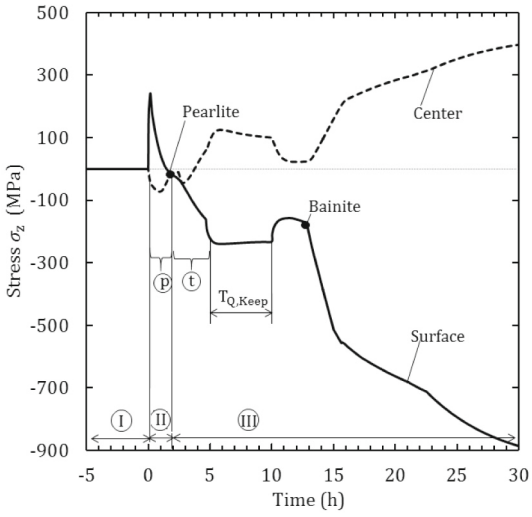

(b) Stress σ_z at inner and outer surfaces when $z = 0$

Fig. A.2. Temperature and stress σ_z in Fig. 2(b).
(a) Temperature at inner and outer surface along $|z| \leq 900$ mm.
(b) Stress σ_z at inner and outer surfaces when $z = 0$.

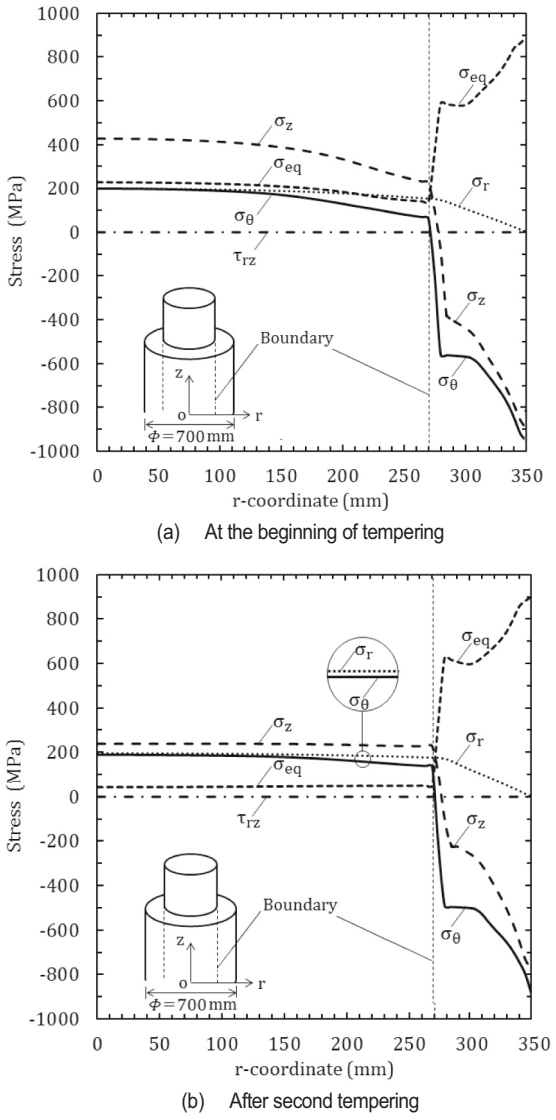

Fig. A.3. All residual stress distribution at $z = 0$ in Fig. 2(b).
(a) At the beginning of tempering.
(b) After second tempering.

Appendix B. Fatigue limit line for the bimetallic solid roll under large compressive stress

In this paper, Sections 3 and 4 treated the residual stress of the bimetallic sleeve roll newly analyzed. Section 5 confirmed the validity of the results in terms of the fatigue strength as shown in Fig. 13 compared to the solid roll [9,17,42–44,57,62]. It should be noted that the solid roll requires fatigue strength under large compressive stress. For the readers' convenience, therefore, this Appendix B will explain the outline of the fatigue limits for the solid roll since no study is available except the authors' previous studies [42,43].

Fig. B.1 shows a stress amplitude versus mean stress diagram (σ_a-σ_m diagram) to discuss the fatigue limit under large compressive alternative loading $\sigma_m \leq 0$.

First of all, assume the ultimate tensile strength σ_B can be applied to the compressive stress $\sigma_m < 0$ and alternative stress $\sigma_a > 0$ as express in Eq. (B.1).

$$|\sigma_m| < \sigma_B, |\sigma_a| < \sigma_B \tag{B.1}$$

The so-called modified Goodman law can be expressed in Eq. (B.2) for $\sigma_m \geq 0$.

$$\frac{\sigma_a}{\sigma_{w0}} + \frac{\sigma_m}{\sigma_B} \leq 1 \tag{B.2}$$

Assume this limit line $\sigma_a/\sigma_{w0} + \sigma_m/\sigma_B = 1$ can be extended to the negative region $\sigma_m < 0$ [73]. Consider pulsating compressive loading $\sigma_a + \sigma_m = \sigma_{max} = 0$ as illustrated in Fig. B.1(c). In Fig. B.1(a), the line is indicated as $\sigma_m = -\sigma_a$ denoted by a dotted line with an angle of 45° from the ordinate to the origin. In the region described by Eq. (B.3), the crack does not propagate and no final failure happens.

$$\sigma_a + \sigma_m = \sigma_{max} \leq 0 \tag{B.3}$$

Denote the intersection $\sigma_a/\sigma_{w0} + \sigma_m/\sigma_B = 1$ and $\sigma_a + \sigma_m = 0$ as point E as shown in Fig. B.1(a). Since point E satisfies Eq. (B.3), there is no final failure. Therefore, by adding a certain amount of positive tensile stress, point F and point F′ are newly considered [74]. Regarding the fully reversed loading, the fatigue limit is known as point D as shown in Fig. B.1(b). Point D can be the fatigue limit under the maximum tensile stress $\sigma_{max} = \sigma_m + \sigma_a = 166$ MPa and the maximum compressive stress $\sigma_{min} = \sigma_m - \sigma_a = -166$ MPa. Instead, at point E, as shown in Fig. B.1(c), the maximum tensile stress $\sigma_{max} = \sigma_m + \sigma_a = 0$ but the maximum compressive stress $\sigma_{min} = \sigma_m - \sigma_a = -554$ MPa is more than three times larger than the compressive stress of point D, $\sigma_{min} = -166$ MPa since $\sigma_{min} = -554$ MPa $= -277$ MPa $\times 2 < -166$ MPa $\times 3 = -498$ MPa. Therefore, at point E, even with no crack propagation and no final failure, more severe damage is accumulated regarding crack initiation compared to point D.

Consider F′ whose maximum tensile stress $\sigma_{max} = 166$ MPa is the same as point D as shown in Fig. B.1(e). Due to the larger compressive stress $\sigma_{min} = -554$ MPa at point E compared to the one $\sigma_{min} = -166$ MPa at point D, the tensile stress necessary for the fatigue limit can be smaller than $\sigma_{max} = 166$ MPa. Instead, at point E, there is no tensile stress, therefore there is no crack propagation and no final failure as the previous studies indicated [75–77]. In this way, it is found that the fatigue limit point F should be between point D and point F′.

In this study, therefore, half value $\sigma_{w0}/2 = 83$ MPa is assumed for this tensile stress at point F as shown in Fig. B.1(d). By drawing the line through point D and point F in Fig. B.1(a), the fatigue limit can be estimated. The range can be expressed by the following Eq. (B.4).

$$\sigma_a \leq -\frac{\sigma_B + \sigma_{w0}}{2\sigma_B}\sigma_m + \sigma_{w0} \tag{B.4}$$

For large compressive alternative loading, the fatigue limit is determined by Eqs. (B.1) to (B.4), which is expressed by the thick solid lines passing through points A, D, F, G, and H in Fig. B.1(a).

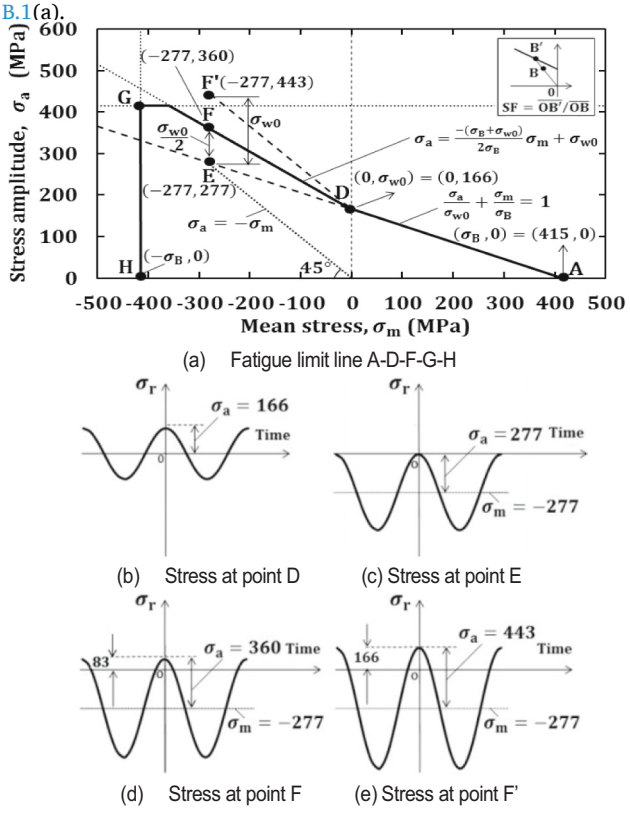

Fig. B.1. Fatigue limit line under large compressive stress.
(a) Fatigue limit line A-D-F-G-H.
(b) Stress at point D.
(c) Stress at point E.
(d) Stress at point F.
(e) Stress at point F′.

References

[1] Shimoda H, Onodera S, Hori K. Study on the residual defection of large sleeved back-up rolls. 4th report, residual stresses of sleeved rolls. Trans Jpn Soc Mech Eng 1966;32:689–94. https://doi.org/10.1299/kikai1938.32.689.

[2] Takigawa H, Hashimoto K, Konno G, Uchida S. Development of forged high-speed-steel roll for shaped steel. CAMP-ISIJ 2003;16:1150–3.

[3] Irie T, Takaki K, Tsutsunaga I, Sano Y. Steel strip and section steel and thick rolling, processing. Tetsu to Hagane 1979;65:293.

[4] Inoue T, Uchida S, Ogawa S. Characteristics of wear and rolling on fiber reinforced metal at high temperature. J Iron Steel Inst Jpn 2015;55:1987. https://doi.org/10.2355/isijinternational.ISIJINT-2015-123.

[5] Hattori T, Kamitani Y, Sugino K, Tomita H, Sano Y. Super cermet rolls for manufacturing ultra-fine-grained steel. In: International conference on tribology in manufacturing processes ICTMP 2007 international conference; 2007. 24–26 September. Yokohama.

[6] Hamayoshi S, Ogawa E, Shimiz K, Noda NA, Kishi K, Koga S. Development of large ceramic rolls for continuous hot-dip galvanized steel sheet production lines. Sokeizai 2010;51(12):54–9. http://hdl.handle.net/10228/00006066.

[7] Mezentsev AV, Il'in VA, Syusyukin AY. Mastering of the technology of assembling of composite mill rolls under the conditions of rail and structural steel shop at the JSC "EVRAZ ZSMK". Metallurgist 2019;63(5):562. https://doi.org/10.1007/s11015-019-00860-5.

[8] Noda NA, Sano Y, Takase Y, Shimoda Y, Zhang G. Residual deflection mechanism for back-up roll consisting of shrink-fitted sleeve and arbor. J JSTP 2017;58(672):66. https://doi.org/10.9773/sosei.58.66.

[9] Noda NA, Sakai H, Sano Y, Takase Y, Shimoda Y. Quasi-equilibrium stress zone with residual displacement causing permanent slippage in shrink-fitted sleeve rolls. Metals 2018;8(12):998. https://doi.org/10.3390/met8120998.

[10] Matsunaga E, Sano Y, Nishida S. Fatigue characteristics of composite sleeve roll inner layer material (strength design of shrink ftted sleeve roll for hot strip mill-1). CAMP-ISIJ 1997;10:1078.
[11] Matsunaga E, Tsuyuki T, Sano Y. Optimum shrink fitting ratio of sleeve roll (strength design of shrink ftted sleeve roll for hot strip mill-1). CAMP-ISIJ 1998;11:362. https://ci.nii.ac.jp/naid/10002551803.
[12] Tutumi S, Hara S, Yoshi S. The residual defection of sleeved backup-up rolls. Tetsu to Hagane 1971;57(5):818–22. https://doi.org/10.2355/tetsutohagane1955.57.5_818.
[13] McMillan MD, Booker JD, Smith DJ, Onisa CF, Korsunsky AM, Song X, et al. Analysis of increasing torque with recurrent slip in interference-fits. Eng Fail Anal 2016;62:58. https://doi.org/10.1016/j.engfailanal.2015.12.005.
[14] Sano Y. Recent advances in rolling rolls. In: Proc of the No. 148–149 Nishiyama Memorial Technology Course. Tokyo, Japan; 1993. p. 193–226.
[15] Sano Y. Fatigue failure problem in the inside of roll body for hot strip rolling - crack initiation problem and its estimation in the actual plant. In: The 245th JSMS Committee on Fatigue of Materials and the 36th JSMS Committee on Strength Design. Safety evaluation. 40; 1999.
[16] Bataille C, Luc E, Bigerelle M, Deltombe R, Dubar M. Rolls wear characterization in hot rolling process. Tribol Int 2016;100:328. https://doi.org/10.1016/j.triboint.2016.03.012.
[17] Noda NA, Hu K, Sano Y, Ono K, Hosokawa Y. Residual stress simulation for hot strip bimetallic roll during quenching. Steel Res Int 2016;87(11):1478. https://doi.org/10.1002/srin.201500430.
[18] Hu K, Xia Y, Zhu F, Noda NA. Evaluation of thermal breakage in bimetallic work roll considering heat treated residual stress combined with thermal stress during hot rolling. Steel Res Int 2017;89(4):1700368. https://doi.org/10.1002/srin.201700368.
[19] Sakai H, Noda NA, Sano Y, Zhang G, Takase Y. Numerical simulation on interfacial creep generation for shrink-fitted bimetallic roll. ISIJ Int 2019;59(5):889. https://doi.org/10.2355/isijinternational.ISIJINT-2018-749.
[20] Sakai H, Noda NA, Sano Y, Zhang G, Takase Y. Effect of driving torque on the interfacial creep for shrink-fitted bimetallic work roll. Tetsu to Hagane 2019;105(12):1126–34. https://doi.org/10.2355/tetsutohagane.TETSU-2019-048.
[21] Noda NA, Rafar RA, Sakai H, Zheng X, Tsurumaru H, Sano Y, et al. Irreversible interfacial slip in shrink-fitted bimetallic work roll promoted by roll deformation. Eng Fail Anal 2021;126:105465. https://doi.org/10.1016/j.engfailanal.2021.105465.
[22] Rafar RA, Noda NA, Tsurumaru H, Sano Y, Takase Y. Novel design concept for shrink-fitted bimetallic sleeve roll in hot rolling mill. Int J Adv Manuf Technol 2022;120:3167. https://doi.org/10.1007/s00170-022-08954-.
[23] Noda NA, Rafar RA, Sano Y. Stress due to interfacial slip causing sleeve fracture in shrink-fitted work roll. Int J Mod Phys B 2021;2140020. https://doi.org/10.1142/S0217979221400208.
[24] Hamid RBR, Ahmad M, Mohd HI, Mohammed RAK, Hassan J. Premature failure analysis of forged cold back-up roll in a continuous tandem mill. Mater Des 2011;32:4376–84. https://doi.org/10.1016/j.matdes.2011.03.078.
[25] Kang X, Li D, Xia L, Campbell J, Li Y. Development of cast steel back-up roll. Int J Cast Met Res 2006;19:66–71. https://doi.org/10.1179/136404606225023327.
[26] Wang D, Rong S. Study on cast-weld process and composite interface of bimetal composite roll sleeve. J Mater Res Technol 2021;12:848–61. https://doi.org/10.1016/j.jmrt.2021.03.032.
[27] Sano Y, Hattori T, Haga M. Characteristics of high-carbon high speed steel rolls for hot strip mill. ISIJ Int 1992;32:1194–201. https://doi.org/10.2355/isijinternational.32.1194.
[28] Soda N. Bearing. Tokyo: Iwanami Shoten; 1964. p. 196–203.
[29] Imai M. Creep of the roller bearing. Lubr J Jpn Soc Lubr Eng 1959;4(6):307.
[30] Murata J, Onizuka T. Generation mechanism of inner ring creep. Koyo Eng J 2005;166:41–7.
[31] Niwa T. A creep mechanism of rolling bearings. NTN Tech Rev 2013;81:100–3.
[32] Sakajiri Ten, Yukawa Takemura. Tech J NSK680; 2006. p. 13.
[33] New Bearing Doctor. Diagnosis of bearing problems. Objective: smooth & reliable operation. NSK; 1997 [accessed 28 June 2020], https://www.nsk.com/common/data/ctrgPdf/e7005c.pdf.
[34] Zhan J, Takemura H, Yukawa K. A study on bearing creep mechanism with FEM simulation. Seattle: Proc Int Mech Eng Congr Expo; 2007. https://doi.org/10.1115/IMECE2007-41366.
[35] Zhan J, Yukawa K, Takemura H. Analysis of bearing outer ring creep with FEM. Adv Tribol Berlin 2009. https://doi.org/10.1007/978-3-642-03653-8_74.
[36] Noguchi S, Ichikawa K. A study about creep between inner ring of ball bearing and shaft. Japan: Proc Acad Lect Jpn Soc Precis Eng; 2010.
[37] Teramoto T, Sato Y. Prediction method of outer ring creep phenomenon of ball bearing under bearing load. Trans Soc Automot Eng Jpn 2015;46:355–60. https://doi.org/10.11351/jsaeronbun.46.355.
[38] Bovet C, Zamponi L. An approach for predicting the internal behaviour of ball bearings under high moment load. Mech Mach Theory 2016;101:1. https://doi.org/10.1016/j.mechmachtheory.2016.03.002.
[39] Maiwald A, Leidich EFE. Simulations of irreversible relative movements (creeping) in rolling bearing seats – influential parameters and remedies. In: Proc World Congr Eng Comput Sci San Fr. 2; 2013. http://www.iaeng.org/publication/WCECS2013/WCECS2013_pp1030-1035.pdf.
[40] Schiemann T, Porsch S, Leidich E, Sauer B. Intermediate layer as measure against rolling bearing creep. Wind Energy 2018;21(4):26. https://doi.org/10.1002/we.2170.
[41] Noda NA, Rafar RA, Taruya Y, Zheng X, Tsurumaru H, Sano Y, et al. Interfacial slip verification and slip defect identification in shrink-fitted bimetallic sleeve roll used in hot rolling mill. Tribol Int 2022;175:107793.
[42] Noda NA, Hu K, Sano Y, Ono K, Hosokawa Y. Residual stress simulation for hot strip bimetallic roll during quenching. Steel Res Int 2016;87:1478–88. https://doi.org/10.1002/srin.201500430.
[43] Noda NA, Hu K, Sano Y, Ono K, Hosokawa Y. Usefulness of non-uniform heating and quenching method for residual stress of bimetallic roll: FEM simulation considering creep behavior. Steel Res Int 2017;88:1600165. https://doi.org/10.1002/srin.201600165.
[44] Noda NA, Sano Y, Aridi MR, Tsuboi K, Oda N. Residual stress differences between uniform and non-uniform heating treatment of bimetallic roll: effect of creep behavior on residual stress. Metals 2018;8:952. https://doi.org/10.3390/met8110952.
[45] Schajer GS. Practical residual stress measurement methods7. Hoboken: John Wiley & Sons; 2013.
[46] Kingston E, Smith DJ. Residual stress measurements in rolling mill rolls using deep hole drilling technique. Ironmak Steelmak 2005;32(5):379–80.
[47] Sachs G. Z Met 1927;19:352.
[48] Higashida Y, Kikuma T, Kawanami T, Kimura K. Measurement method of residual stress of rolls and countermeasure to thermal stress breaking. In: Tetsu-to-Hagane. Shaping & fabrication • instrumentation & control, The 111th ISIJ meeting. 72; 1986. p. 308.
[49] Costa Neto AF, Barbosa CA, Dialetachi F. X-Ray diffraction technique applied to manufacture and control of rolling mill rolls. In: 34th mechanical working and steel processing conference. Vol. XXX. Warrendale (PA): Iron and Steel Society of AIME; 1993. p. 199–203.
[50] Kokosza A, Pacyna J, Wojtas A. Residual stress measurement in steel mill rolls using magnetic Barkhausen noise analysis. J Nondestr Test 1999;4(8). https://www.ndt.net/?id=446.
[51] Yasuhiro J. Study on residual stress measurement of roll for rolling mill. In: 33rd mechanical working and steel processing conference. Vol. XXIX. Warrendale (PA): Iron and Steel Society of AIME; 1992. p. 187.
[52] Kang SH, Im YT. Thermo-elasto-plastic finite element analysis of quenching process of carbon steel. J Mater Process Technol 2007;192–193:381–90. https://doi.org/10.1016/j.jmatprotec.2007.04.101.
[53] Majorek A, Scholtes B, Müller H, Macherauch E. Influence of heat transfer on the development of residual stresses in quenched steel cylinders. Steel Res 1994;65(4):146–51. https://doi.org/10.1002/srin.199400944.
[54] Sun CG, Kim JW, Hwang SM. Investigation of the thermo-mechanical behavior of type 304 stainless slab in hot charge rolling condition by the finite element method. ISIJ Int 2003;43(11):1773–80. https://doi.org/10.2355/isijinternational.43.1773.
[55] Arimoto K, Ikuta F, Horino T, Tamura S, Narazaki M, Mikita Y. Preliminary study to identify criterion for quench crack prevention by computer simulation. Trans Mater Heat Treat 2004;25(5):486–93.
[56] Neira Torres I, Gilles G, Tchoufang Tchuindjang J, Flores P, Lecomte-Beckers J, Habraken AM. FE modeling of the cooling and tempering steps of bimetallic rolling mill rolls. Int J Mater Form 2017;10:287–305. https://doi.org/10.1007/s12289-015-1277-0.
[57] Noda NA, Aridi MR, Torigoe R, Tsuboi K, Sano Y. Reduction of residual stress in bimetallic work roll by tempering. J Technol Plastic 2020;61(716):183–1201.
[58] Garcia-Granada AA, Smith DJ, Pavier MJ. A new procedure based on Sachs's boring for measuring non-axisymmetric residual stresses. Int J Mech Sci 2000;42(6):1027–47. https://doi.org/10.1016/S0020-7403(99)00039-9.
[59] Kamimiyada K, Konno Y, Yanagitsuru A. Effect of heating conditions before quenching on residual stress in high-speed steel type cast iron rolls by centrifugal cast. Mater Trans 2020;61(10):1987–93. https://doi.org/10.2320/matertrans.F-M2020841.
[60] Hamada S, Sakoda Y, Sasaki D, Ueda M, Noguchi H. Evaluation of fatigue limit characteristics of lamellar pearlitic steel in consideration of microstructure. Soc Mater Sci Jpn 2011;9(9):790–5.
[61] Sente Software - JMatPro® https://www.sentesoftware.co.uk/jmatpro.
[62] Noda NA, Aridi MR, Sano Y. Tempering effect on residual stress in bimetallic roll. Int J Mod Phys B 2021;35:2140044. https://doi.org/10.1142/S0217979221400440.
[63] May DL, Gordon AP, Segletes DS. The application of the Norton-Bailey law for creep prediction through power law regression. San Antonio, Texas, USA: Proc. Of ASME Turbo Expo; 2013. p. 1–8. https://doi.org/10.1115/GT2013-96008.
[64] WO2013042528 A1. Centrifugal casted composite roller for hot rolling and method for producing same. https://patents.google.com/patent/WO2013042528A1/ja; 2012.
[65] Tanaka Z, Obata T. A study on stress relief heat treatment (report II)-the relation between isothermal relaxation and isothermal relaxation creep of HT60. J Jpn Weld Soc 1967;36(3):222–8. https://doi.org/10.2207/qjjws1943.36.222.
[66] Marc Mentat team. Theory and user informationVol. A. Tokyo: MSC. Software; 2012.
[67] Ohtani R. High temperature strength of structure (V) creep strength and creep rupture strength. Jpn Soc Mater Sci Jpn 1969;18:824–30. https://doi.org/10.2472/jsms.18.824.
[68] Sakai T, Lian B, Takeda M, Shiozawa K, Oguma N, Ochi Y, et al. Statistical duplex S-N characteristics of high carbon chromium bearing steel in rotating bending in very high cycle regime. Int J Fatigue 2010;32:497–504. https://doi.org/10.1016/j.ijfatigue.2009.08.001.

[69] Zalnezhad E, Sarhan AAD, Jahanshahi P. A new fretting fatigue testing machine design, utilizing rotating-bending principle approach. Int J Adv Manuf Technol 2014;70:2211–9. https://doi.org/10.1007/s00170-013-5457-0.
[70] Schroder KH. A basic understanding of the mechanics of rolling mill rolls. Tenneck, Austria: Eisenwerk Sulzau-Werfen, ESW-Handbook; 2003.
[71] Aridi MR, Noda NA, Sano Y, Takata K, Zifeng S. Effect of the residual stress to the fatigue failure of the bimetallic work roll in 4-high rolling mill. Springer Proc. In: Parinov IA, Chang SH, Kim YH, Noda NA, editors. Materials. vol. 10. Switzerland: Springer Nature; 2020. p. 389–93.
[72] Noda NA, Rafar RA, Taruya Y, Zheng X, Tsurumaru H, Sano Y, et al. Fatigue strength analysis of bimetallic sleeve roll by simulation of local slip accumulation at shrink-ft interface caused by roll rotation. Int J Adv Manuf Technol 2022;125:369–85. https://doi.org/10.1007/s00170-022-10669-3.
[73] Ince A, Glinka G. A modification of morrow and Smith-Watson-Topper mean stress correction models. Fatigue Fract Eng Mater Struct 2011;34:854–67. https://doi.org/10.1111/j.1460-2695.2011.01577.x.
[74] Kasaba K, Sano T, Kudo S, Shoji T, Katagiri K, Sato T. Fatigue crack growth under compressive loading. J Nucl Mater 1998;258–263:2059–63. https://doi.org/10.1016/S0022-3115(98)00343-2.
[75] Nishitani H, Yamashita N. Effect of mean stress on initiation and growth of fatigue crack in 70/30 brass. Trans JSME 1996;32:1456–61. https://doi.org/10.1299/kikai1938.32.1456.
[76] Nisitani H, Goto M. Effect of mean stress on initiation and initial growth of fatigue crack in tension compression fatigue of annealed S45C. Trans JSME Part A 1984;50:1926–35. https://doi.org/10.1299/kikaia.50.1926.
[77] Akiniwa Y, Tanaka K, Taniguchi N. Propagation and non-propagation of short fatigue cracks in notched low-carbon-steel specimen under cyclic compression. Trans JSME Part A 1987;53:1768–74. https://doi.org/10.1299/kikaia.53.1768.